THE JOURNAL OF BIOLOGICAL CHEMISTRY VOL. 286, NO. 1, pp. 649–660, January 7, 2011

Constraint-based, Homology Model of the Extracellular Domain of the Epithelial Na^+ Channel α Subunit Reveals a Mechanism of Channel Activation by Proteases*[S]

Received for publication, July 21, 2010, and in revised form, September 22, 2010 Published, JBC Papers in Press, October 25, 2010, DOI 10.1074/jbc.M110.167098

Ossama B. Kashlan[‡], Joshua L. Adelman[§], Sora Okumura[‡], Brandon M. Blobner[‡], Zachary Zuzek[‡], Rebecca P. Hughey[‡¶], Thomas R. Kleyman[‡¶1], and Michael Grabe[§‖2]

From the Departments of [‡]Medicine, [§]Biological Sciences, [¶]Cell Biology and Physiology, and [‖]Computational and Systems Biology, University of Pittsburgh, Pittsburgh, Pennsylvania 15261

The epithelial Na^+ channel (ENaC) mediates Na^+ transport across high resistance epithelia. This channel is assembled from three homologous subunits with the majority of the protein's mass found in the extracellular domains. Acid-sensing ion channel 1 (ASIC1) is homologous to ENaC, but a key functional domain is highly divergent. Here we present molecular models of the extracellular region of α ENaC based on a large data set of mutations that attenuate inhibitory peptide binding in combination with comparative modeling based on the resolved structure of ASIC1. The models successfully rationalized the data from the peptide binding screen. We engineered new mutants that had not been tested based on the models and successfully predict sites where mutations affected peptide binding. Thus, we were able to confirm the overall general fold of our structural models. Further analysis suggested that the α subunit-derived inhibitory peptide affects channel gating by constraining motions within two major domains in the extracellular region, the thumb and finger domains.

Epithelial Na^+ channels (ENaCs)[3] are members of the ENaC/degenerin family of ion channels, of which the high resolution structure of acid-sensing ion channel 1 (ASIC1) has been reported. These channels are probably trimers (1, 2) with each subunit having two transmembrane helices, large extracellular regions, and short cytosolic amino and carboxyl termini (3). The resolved structure of the extracellular region of ASIC1 is composed of core β-sheet domains (termed palm and β-ball) surrounded by peripheral α-helical domains (termed finger, thumb, and knuckle) (1). Channels in the ENaC/degenerin family are Na^+-permeable and are gated by a diverse set of stimuli, including external ligands and mechanical forces (4). As such, ENaC/degenerin family members play diverse roles in biology. For ENaC, these include the regulation of extracellular volume and blood pressure by mediating Na^+ transport in the distal nephron of the kidney, regulation of airway surface liquid volume and mucociliary clearance by facilitating Na^+ transport in airways, and facilitation of salt taste by transporting Na^+ in lingual epithelium (4). ENaC is assembled from homologous α, β, and γ subunits and is allosterically inhibited by extracellular Na^+ by a phenomenon referred to as Na^+ self-inhibition (5–7). Within the ENaC/degenerin family, sequence conservation is conspicuously lacking within the finger domains of the extracellular regions of these channels (1). This fact may partly account for the diversity in the regulation of channel gating observed among gene family members and is an obstacle in building comparative models of ENaC subunits based on the resolved ASIC1 structure.

Among the panoply of ENaC properties is its activation by proteolytic cleavage, which is unusual for ion channels (8). Proteolytic activation of ENaC occurs through the cleavage of both the α and γ subunits at multiple sites within their finger domains, leading to the release of inhibitory tracts (9–12). Peptides corresponding to these inhibitory tracts are also inhibitory (9, 11, 13, 14). Cleavage of the α subunit at two defined sites by the proprotein convertase furin occurs in the *trans*-Golgi network (10). In contrast, furin cleaves the γ subunit once (10). A second protease, such as prostasin, elastase, or plasmin, activates channels by cleaving the γ subunit at sites distal to the furin site (11, 15, 16). It is becoming clear that aberrant proteolysis of ENaC contributes to the enhanced channel activity observed in cystic fibrosis and proteinuric kidney diseases. In cystic fibrosis, enhanced ENaC activity leads to drying of the airways and mucociliary dysfunction (17–19). In the kidney, glomerular injury allows for the filtration of ENaC-activating proteases that are not usually found in the urinary space, contributing to the enhanced renal Na^+ reabsorption and edema observed in proteinuric states (4, 9, 15, 20, 21).

Although proteases activate ENaC by cleaving specific subunits and releasing inhibitory tracts, the structural basis for channel activation by proteases has not been elucidated. In an earlier work (22), we identified a number of sites where mutations altered the apparent affinity of an inhibitory peptide

* This work was supported, in whole or in part, by National Institutes of Health Grants DK078734 (to O. B. K.), DK051391 (to T. R. K.), DK065161 (to T. R. K. and R. P. H.), and DK079307 (to the Pittsburgh Center for Kidney Research). This work was also supported by a Scientist Development Grant from the American Heart Association (to O. B. K.) and a National Science Foundation Career Award MCB0845286 (to M. G.).

[S] The on-line version of this article (available at http://www.jbc.org) contains supplemental Fig. S1 and Movie S1.

[1] To whom correspondence should be addressed: Renal-Electrolyte Division, A919 Scaife Hall, 3550 Terrace St., Pittsburgh, PA 15261. E-mail: kleyman@pitt.edu.

[2] An Alfred P. Sloan Research Fellow.

[3] The abbreviations used are: ENaC, epithelial Na^+ channel; ASIC1, acid-sensing ion channel 1; P8, Ac-LPHPLQRL-amide; r.m.s., root mean square; MTS-4-MTS, 1,4-butanediyl bismethanethiosulfonate.

derived from the α inhibitory tract. To date, ASIC1 is the only member of the ENaC/degenerin gene family whose molecular structure has been determined (Fig. 1) (1, 23). It has been proposed that ligand binding events in the finger and thumb domains translate to motions in the pore via the thumb domain, which is situated to exert a force on the wrist and transmembrane regions (1). The finger domains are highly variable among ENaC/degenerin family members. This sequence variability may be related to the ability of these channels to transduce a diverse set of extracellular signals to channel opening or closing (4, 24). The finger domain appears to have a critical role in the allosteric mechanisms by which responses to external cues lead to movements at the much more highly conserved transmembrane helices over 20 Å away.

To further understand the process by which external cues regulate ENaC/degenerin channels, particularly with regard to ENaC activation by proteases, we built models of α ENaC based in part on homology to ASIC1. α ENaC has modest sequence identity to ASIC1 throughout most extracellular domains. However, identity is particularly poor in the finger domain, where α ENaC has 73 additional residues. To determine the molecular architecture of the α ENaC finger domain, we generated distance constraints from our inhibitory peptide binding data (22). Here, we present data that support the hypothesis that the furin-excised α inhibitory tract and the inhibitory tract-derived peptide bind a common site. Models were constructed and assessed for their quality and ability to account for peptide binding data. We tested an additional region of α ENaC that our models predicted to be in close proximity to the peptide binding site. These experiments identified additional sites that attenuated peptide inhibition, providing a confirmation of our models. We used normal mode analysis to examine differences in motion elicited by an inhibitory peptide. We found that the inhibitory peptide reduced motions in the finger domain near the finger-thumb interface in our model. Based on our results, we propose that the release of the α subunit inhibitory tract relieves constraints at the finger and finger-thumb interface, allowing for movements of the thumb and/or finger domains that facilitate channel transitions to an open, or conducting, state.

EXPERIMENTAL PROCEDURES

Site-directed Mutagenesis, Oocyte Expression, and Two-electrode Voltage Clamp—Site-directed mutations in mouse α, β, and γ ENaC subunits were generated using QuikChange II XL (Stratagene, La Jolla, CA), using cDNAs in pBluescript SK(-) vector as template. We mutated α ENaC residues 211–218 to AEAEEAEA in two steps, first mutating residues 211–214 and then adding in mutations 215–218. Sequencing was performed to confirm the mutation. ENaC expression in *Xenopus laevis* oocytes, and two-electrode voltage clamp were performed as described (22). Peptides were obtained from GenScript USA Inc. (Piscataway, NJ).

Statistical Analysis—Comparisons of significance between groups were performed with a non-linear mixed regression model analysis (see Ref. 22) or analysis of variance, as indicated.

Modeling—Sequence alignment was performed using ClustalX with the BLOSUM62 scoring matrix (25). Secondary structure prediction was performed using PROF (26), SSPro (27), PSIPRED (28), the PredictProtein server (29), and JPred 3 (30) using default parameters. Comparative modeling was performed using MODELLER (31). For each model, we computed the surface accessibility and residue-residue distances with the program DeepView (32). The MMTSB Tool Set (33) was used to cluster models by root mean square (r.m.s.) deviation after carrying out superpositions. Cytoscape (34) was used to generate the clustering diagram, and all molecular figures were generated with PyMOL (DeLano Scientific, LLC, Palo Alto, CA). Coordinates for generated models are provided in the supplemental material.

Calculation of C_α-C_α Distances—To determine the α carbon to α carbon (C_α-C_α) distances that define the shells of interaction for a given residue, the C_α-C_α distance of all C_α-C_α pairs in a number of proteins was measured using DeepView (32). Because we are interested in the packing of residues that are distant in primary sequence, we excluded C_α-C_α pairs from the 10 nearest sequence neighbors. The C_α-C_α distance between interacting, non-neighboring residues should be a general property of all proteins, dependent on local non-covalent packing interactions. A histogram with a bin size of 0.01 Å was generated and normalized by dividing the frequency value of each bin by its volume using Igor Pro. Redoing the analysis with only a few proteins indicates that the radial distribution of distances converges. The data were fit by a sum of 10 Gaussian curves,

$$f(x) = \sum_{i=1}^{10} A_i e^{-\left(\frac{x-\mu_i}{2\sigma_i}\right)^2} \quad \text{(Eq. 1)}$$

where A represents the amplitude, μ is the peak position, and σ is one-half of the peak width. To reduce the number of fit parameters from 30 to 13, we postulated that the peak positions are regularly spaced and that the peak widths increase in proportion to their peak's distance from the origin. For each peak, we used the following relationships.

$$\mu_i = i\mu_1\Delta_\mu \quad \text{(Eq. 2)}$$

$$\sigma_i = \sigma_1\frac{\mu_i}{\mu_1} \quad \text{(Eq. 3)}$$

Three parameters, μ_1, σ_1, and Δ_μ, then determine μ and σ for all peaks, where Δ_μ is the peak spacing. Peak amplitudes were allowed to float independently. The fit was poor at the beginning of the first peak, where all residuals are negative. Allowing all 30 parameters to float independently did not improve the fit.

Normal Mode Analysis—We carried out normal mode analysis on our structural models using the Anisotropic Network Model Web server (35). The model assumes that all C_α atoms within a specified cut-off distance are attached by uniform springs. The equilibrium distance between the atoms is then determined from the initial structure. The topology of the protein complex along with the cut-off distance and

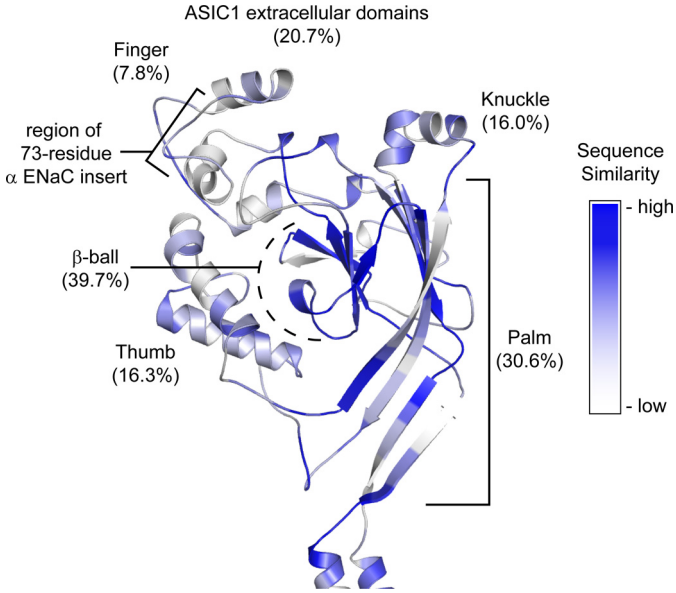

FIGURE 1. **ASIC1 extracellular domains and their homology to ENaC α subunit.** The extent of sequence identity between chicken ASIC1 and mouse α ENaC is indicated in *parentheses*. Sequence alignment was performed as described under "Experimental Procedures." Residues that were identical, similar, or non-homologous were assigned scores of 1, 0.5, or 0, respectively. A 5-residue moving average was then calculated and used to *color* the schematic as indicated.

spring constant specify the potential energy of the system and the subsequent dynamics (see Refs. 35 and 36 for a more detailed description). In the present set of calculations, we used a uniform spring constant of 1 kcal/mol/Å^2 and a cut-off distance of 15 Å.

RESULTS

α ENaC Homology to ASIC1—ASIC1 has low overall homology to ENaC subunits (17–20% identity and 28–31% similarity, using alignments based on the BLOSUM62 substitution matrix). These values place a comparative model of ENaC subunits based on ASIC1 in the "twilight zone," where modeling of a protein with less than 30% sequence identity can result in serious errors in the predicted fold (37). However, ASIC1 and ENaC subunits clearly belong to the same superfamily (38), and there are many instances of proteins within superfamilies that adopt the same fold despite sequence identity on the order of 10% (*e.g.* Na^+-driven transporters (39)). Furthermore, sequence identity between α ENaC and ASIC1 is unevenly distributed. Excluding the finger domain, which is the least conserved, the extracellular domains of ASIC1 share modest sequence similarity with the corresponding domains of α ENaC (25% identity, 37% similarity; Fig. 1). Of these, the β-sheet-dominated palm and β-ball domains are well conserved and located closest to the 3-fold symmetry axis of the extracellular domains, suggesting that the channel core and trimeric arrangement are conserved. Furthermore, the ASIC1 thumb domain is characterized by two helices held together by several disulfide bonds, features predicted for ENaC thumb domains (see below, and see Ref. 40). These observations suggest that these proteins adopt a common fold but that there may be structural divergence in peripheral regions, such as the loops (for further discussion see Ref. 41). Stockand *et al.* (42) presented a model of human α ENaC based on ASIC1; however, areas with limited sequence similarity were removed from the model. This included a large part of the finger domain and resulted in a model of the α ENaC finger domain that recapitulated the structure of the ASIC1 finger domain. This limits the utility of the Stockand model to study ENaC properties that involve the finger domain. This is particularly relevant to the activation of channel by proteases, where cleavage at specific sites in the finger domain releases an intrinsic inhibitory tract. This is also relevant to the inhibition of channels by external Na^+ because selected mutations in the finger domain have dramatic effects on Na^+ self-inhibition.

To characterize the divergent finger domain, we considered our previous finding that furin activates ENaC by cleaving the α subunit twice, removing a 26-residue tract between the cleavage sites at Arg^{205} and Arg^{231} (9). A synthetic peptide corresponding to this tract is inhibitory (9). We hypothesized that the peptide binds to a site analogous to that occupied by the 26-residue tract prior to cleavage. Consistent with this notion, we found that the peptide is a poor inhibitor of channels with non-cleaved α subunits (9). The shorter 8-mer peptide Ac-LPHPLQRL-amide, which we refer to as P8, corresponds to residues 6–13 of the 26-mer and retains the longer peptide's inhibitory properties (13). We identified several sites at which mutation to Trp weakened P8 binding (22). These sites were found throughout the latter half of the finger and in a narrow range at the top of the thumb. We have used these data to provide restraints on the finger domain to complement cASIC1 homology-based restraints for the rest of the extracellular region.

Select Trp Mutants Can Open Channels with Tethered Inhibitory Tracts—We first examined whether P8 and the intrinsic α subunit inhibitory tract share a common binding site. If P8 and the α inhibitory tract bind a common site, models built using P8 binding data are likely to be relevant to the α subunit with an intact inhibitory tract. We know that double cleavage of the α subunit by furin leads to the putative release of residues 206–231, giving rise to increased ENaC activity (9, 10, 12) (see Fig. 2*A*). Mutating either the amino- or carboxyl-terminal furin cleavage site results in a tethered α subunit inhibitory tract where channels remain inactive (9, 12). We postulated that selectively introducing bulky Trp residues at sites that weakened P8 binding would dislodge the tethered inhibitory tract from its initial site and rescue the activity of the tethered mutant channels (Fig. 2*A*). Furthermore, mutating residues that interact at sites within the furin-cleaved fragment that are not within the P8 tract might also rescue channel activity. We mutated the distal furin site (αR231A) to tether the inhibitory tract and judiciously chose the sites to introduce Trp residues based on our results regarding P8 binding (22). In an attempt to maximally displace the tethered inhibitory tract, we mutated tract residues 211–218 from LPHPLQRL to AEAEEAEA, which led to fully active channels despite tethering (Fig. 2*B*). We further examined whether mutations at potential P8 binding sites would displace the tethered tract, resulting in channel activation. Four mutants that exhibited weakened P8 binding (αG252W,

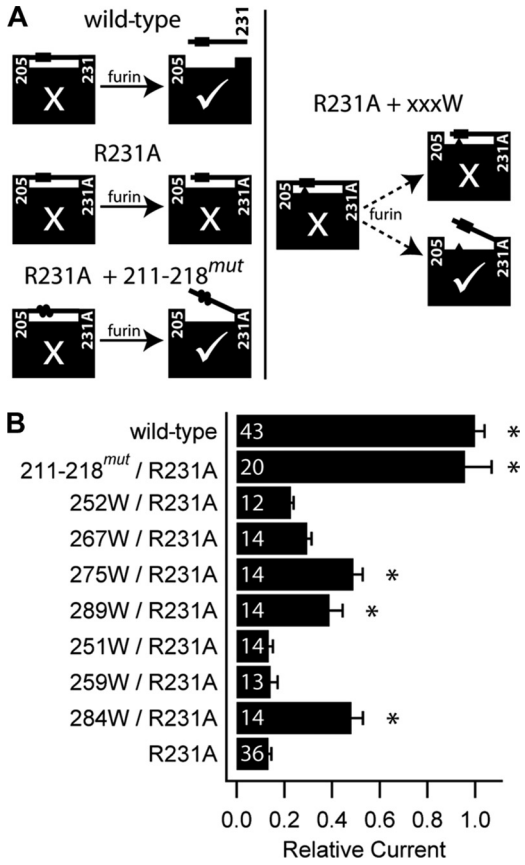

FIGURE 2. **Selected Trp mutants rescue the ENaC αR231A furin-site mutant.** *A*, wild-type ENaC requires furin cleavage at both α-Arg^{205} and α-Arg^{231} for channel activation (*top left*; *X* indicates inactive channels, and *check mark* indicates active channels) (9). Mutation at either furin site results in a largely inactive channel (*middle left*). This phenotype can be rescued by mutation of 211–218 from LPHPLQRL to AEAEEAEA (*211–218^{mut}*) in the inhibitory tract (*bottom left*) or by Trp mutants that displace the 26-mer inhibitory tract from its effector site (*right*). *B*, effects of mutations on ENaC with an αR231A furin site mutant. cRNAs for wild-type and mutant α subunits were co-injected with wild-type β and γ ENaC cRNAs and assayed 24 h after injection. Amiloride-sensitive currents were normalized to wild-type channel currents recorded on the same day. Values are mean ± S.E., *n* is indicated on each *bar*. *p* values were determined by analysis of variance with a Newman-Keuls *post hoc* test. *, $p < 0.005$ *versus* R231A.

αT267W, αV275W, and αR289W) as well as three mutations that had no effect on P8 binding (αI251W, αN259W, and αI284W) were examined (22). In channels that retained their furin cleavage sites, these seven mutations had minimal effects on amiloride-sensitive currents (data not shown). With the distal furin site removed (αR231A), three mutants (αV275W, αR289W, and αI284W) exhibited increased amiloride-sensitive currents compared with αR231A ($p < 0.005$). These results suggest that these Trp mutations at these three sites displace the tethered inhibitory tract. Two of these mutants also weakened P8 affinity (αV275W and αR289W), consistent with the hypothesis that P8 and the inhibitory tract have overlapping binding sites. The αI284W mutant, which did not weaken P8 affinity, may interact with the tethered inhibitory tract at a site distinct from residues 211–218.

Construction of α ENaC Structural Model—To build models of the extracellular region of α ENaC, we made two major assumptions. First, the extracellular region of α ENaC (except the finger) is homologous to the resolved structure of ASIC1 (Fig. 1). Second, P8 binds ENaC at a site analogous to that occupied by residues 211–218 in the non-cleaved α subunit. We used MODELLER to construct the models (31). We implemented homology-based restraints using the alignment in Fig. 3*A* and the ASIC1 structure (Protein Data Bank code 2QTS, chain B) (1). The calculated alignment was manually adjusted to accommodate several small insertions or deletions (see Fig. 3). We implemented P8 binding data-based restraints by requiring that the C_α atom of residues implicated in P8 binding be less than a fixed distance from the corresponding C_α atom(s) in the inhibitory tract. Although these restraints complement homology-based restraints, Reddy and Kaznessis (43) have shown that solely using a low density of C_α-C_α distance restraints (<30% of residues) is insufficient to generate good models. To determine what this restraint distance should be, we calculated the radial distribution of C_α-C_α distances for all residue pairs within 10 model proteins excluding pairs less than 10 residues apart in their primary sequences (Fig. 3*B*). There are two clear shells of interaction, and we fit the distribution with a sum of Gaussians to define the outer limits of the first shell as 7.1 Å and the second shell as 11.7 Å. Sites implicated in P8 binding were restrained to be within 11.7 Å of 211–218, and sites at which a mutation weakened peptide binding more than 10-fold were restrained to be within 7.1 Å of 211–218 (22). Three specific restraints of 7.1 Å between Gln^{254} and Leu^{218}, Arg^{289} and His^{213}, and Asp^{473} and His^{213} were included in our model based on pairwise interactions identified in double mutant cycle experiments (22).

In addition, predicted secondary structures were used to constrain portions of the finger domain that lacked homology to ASIC1 (see "Experimental Procedures"). A disulfide bond was included between Cys^{256} and Cys^{263}. These Cys residues were predicted to flank β-strands, forming an antiparallel β-sheet. Outside the finger domain, extracellular disulfide bonds are conserved between ASIC1 and α ENaC. These Cys pairs were constructed using homology-based restraints with the exception of one pair at the base of the thumb, for which we manually adjusted the alignment and included an explicit restraint (see Fig. 3). In addition, there was poor consensus regarding the length of the predicted finger domain α2 helix (residues 271–289). We built models assuming either a long α2 (residues 271–289) or a more ASIC1-like short α2 helix (residues 271–281; see Fig. 3*A*).

As a starting point for model building, we built initial models of α ENaC based solely on alignment to ASIC1, which included four different finger domain alignments (Fig. 4*A*). The models from each alignment were clustered by assessing the r.m.s. deviation between specific sets of atoms in order to select three structurally distinct models from each alignment (33). One representative from each cluster was then used as an initial model to build 100 models using the Fig. 3*A* alignment and experimental restraints outlined above. We scored each resulting model based on the MODELLER objective function, satisfaction of our data-based restraints, and the accessibility of residues in P8 (positions 211–218). We found that four of the 12 initial models led to subsequent models that scored well using both the long and short α2 assumptions (Fig. 4*B*), and we proceeded to construct 2500 models using

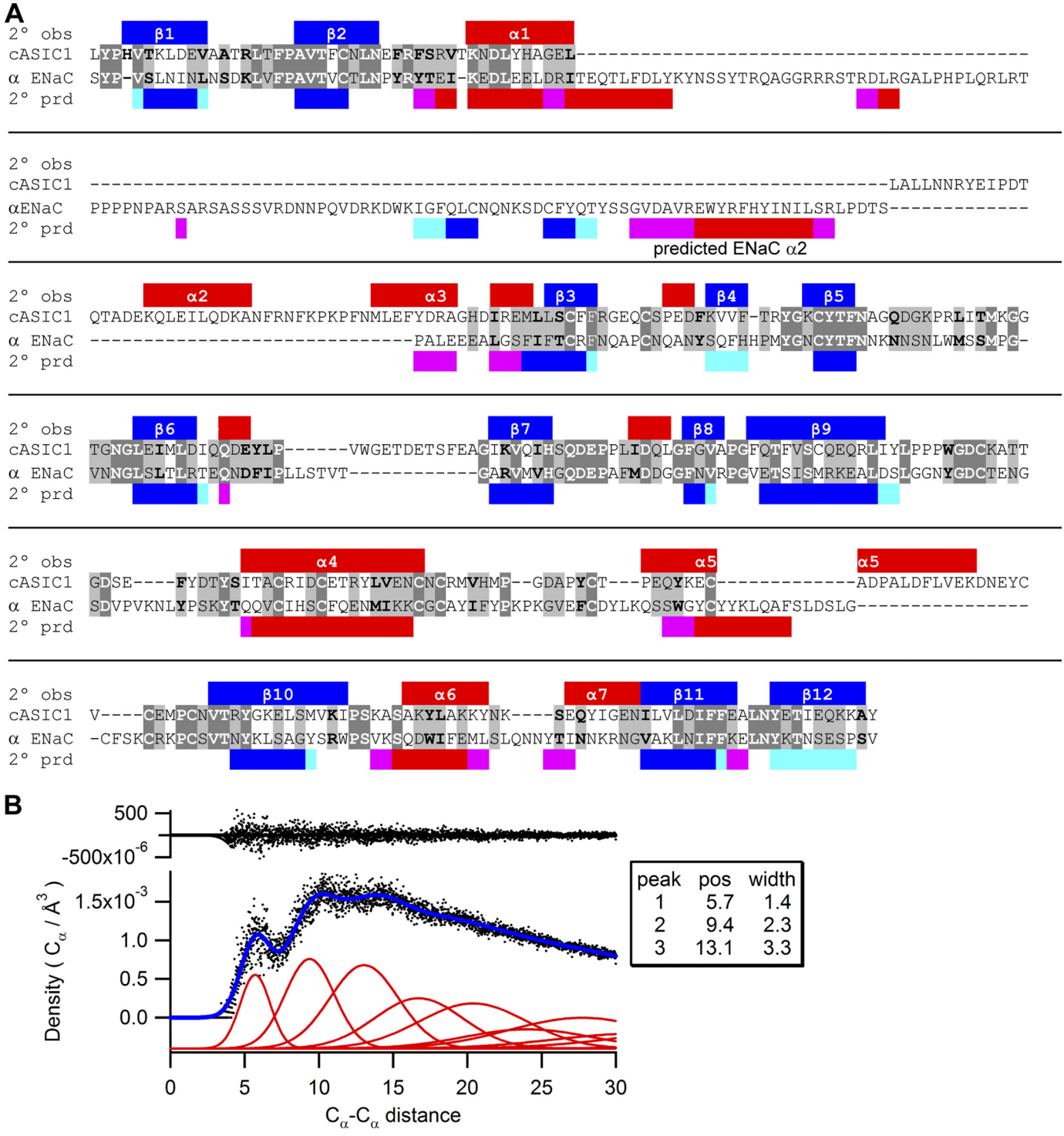

FIGURE 3. **Restraints for α ENaC model building.** *A*, sequence alignments of chicken ASIC1 and mouse α ENaC generated using ClustalW with a BLOSUM62 scoring matrix followed by manual adjustment. Identity (*dark gray background*, *white type*), strong similarity (*light gray background*, *boldface type*), and weak similarity (*light gray background*) are indicated. Resolved secondary structures for ASIC1 and predicted secondary structures (see "Experimental Procedures") for α ENaC are shown. *Blue* and *red* indicate β-strands and α-helices, respectively, with strong consensus (agreement of 4–5 of 5 algorithms). *Turquoise* and *pink* indicate β-strands and α-helices, respectively, with weak consensus (agreement of 2–3 of 5 algorithms). There are three short inserts for which we adjusted the alignment so that they are placed between secondary structures (β9-α4 and α4-α5 in the thumb, and α6-α7 in the knuckle). The β6-β7 loop, which interacts with the finger domain, is longer in ASIC1 than in α ENaC and was not aligned to ASIC1 to avoid constraining the finger domain where sequence identity is poor. The thumb domain is composed of α4 and α5, which are held together by five conserved disulfide bonds. ASIC1 α5 is longer than that predicted for the equivalent helix in α ENaC. In addition, the arrangement of Cys residues following α5 is different between the two channels. Therefore, we did not align α ENaC to the latter half of ASIC α5 and part of the following loop but instead used α helical restraints to complete α5 and constructed the experimentally predicted disulfide bonding pattern (40). *B*, radial distribution of C_α-C_α distances from 10 selected proteins. The Protein Data Bank codes for the 10 proteins are 1MQL, 1N1H, 2QTS, 2HPM, 1VYK, 1JR8, 2FUK, 1S2B, 1M8S, and 2HCB. Data were fit to a sum of Gaussian curves. Sum (*blue*) and component (*red*) Gaussian curves are shown. Residuals of the fit to the data are also shown (*top*).

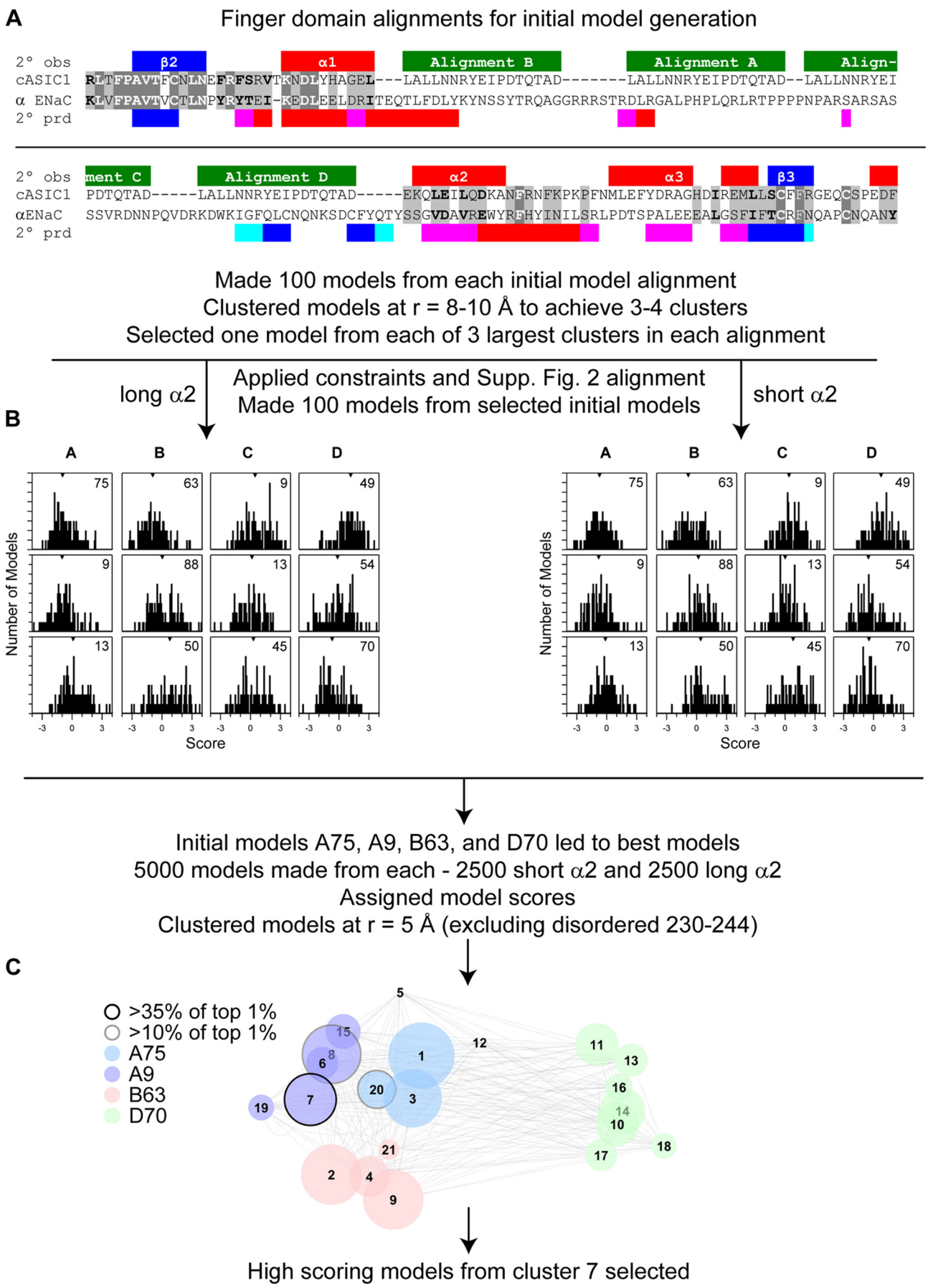

each of the α2 assumptions and each of the four selected initial models as a starting point. We scored each resulting model as before and clustered all models at a radius of 5 Å. Residues 230–244 were excluded from the calculation of each r.m.s. deviation when clustering because this region is predicted to be disordered by DISOPRED (44). These 20,000 resulting models clustered into 21 groups of various sizes, with both long α2 and short α2 models comprising most clusters (Fig. 4*C*). Three of these clusters combined to contain 60.5% of the top scoring 1% of models, with cluster centroids that were similar to each other (mean r.m.s. deviation of 3.7 Å). The best cluster had 37% of the top scoring 1% of models. High scoring models from this cluster with a short α2 (Fig. 5, *B* and *C*) and a long α2 (Fig. 5, *D* and *E*) were selected. These models were evaluated using ProSA (45, 46), which scored our selected models within the range of published high resolution structures of similar size.

α ENaC Structure Model—Our best long α2 and short α2 models of α ENaC, selected on the basis of model quality and restraint satisfaction, are quite similar to ASIC1 while still satisfying the constraints laid out above. The C_α r.m.s. deviation for each of the selected and optimized models with respect to ASIC1 is ~3 Å (Fig. 5*A*). Each model is organized into domains as described for ASIC1 (Fig. 1 and supplemental Fig. S1). The finger domain presents the most notable difference between our α ENaC models and ASIC1 but remains organized around three helices similar to ASIC1. In addition, the α ENaC finger domain is organized so that sites that affected P8 binding are in close proximity to residues 211–218 (Fig. 5, *B*–*E*). According to these models, residues 211–218 are tucked under α2 and may interact with the small antiparallel β-sheet formed between residues 251 and 268. Further, relative to the position of α2 in cASIC1, α2 in both of our models is displaced toward the thumb domain. This is a direct consequence of distance constraints between His^{213} in the inhibitory tract and both Arg^{289} at the end of α2 and Asp^{473} at the top of the thumb, based on our double mutant cycle data (22). Our models suggest that residues 211–218, which correspond to P8, primarily occupy a site defined within the finger domain and also interface with the thumb domain. Our models also place the two furin cleavage sites, Arg^{205} and Arg^{231}, at exposed locations on the surface of the molecule. Interestingly, sites where mutations changed Na^+ self-inhibition line one face of helix α2 in the long α2 model (Fig. 6*A*, *green spheres*). This supports a preference for the model constructed with a long α2.

Functional Test of the α ENaC Model—Our best models suggest that P8 interacts with residues at the very beginning of the finger before α1 and extend into its amino-terminal end (Fig. 6*B*). Such a prediction is not afforded by the Stockand model because large parts of the finger domain are absent, including residues corresponding to P8 (42). We therefore mutated corresponding residues 166–174 (*orange stretch* in *B*) within this region to Trp and measured the inhibition of the mutant channels by 10 μM P8 (Fig. 6*C*). These data were analyzed, taking into consideration indirect effects of mutation on P8 inhibition through changes in channel P_O (see Ref. 22). The Trp scan revealed three more sites that significantly reduced P8 inhibition (*red bars* in Fig. 6*C*).

Notably, a mutation at Glu^{174} was found to influence P8 binding, but it had the weakest effect of the new sites. Therefore, to further examine whether Glu^{174} lies in close proximity to the bound inhibitory peptide, we attempted to cross-link the peptide to the channel. To do this, we introduced a Cys at Glu^{174} in the channel (or at Glu^{173} as a control) and placed a Cys within the peptide. We then used 1,4-butanediyl bismethanethiosulfonate (MTS-4-MTS), a bifunctional Cys-reactive reagent, to attempt to cross-link the peptide to the introduced Cys residue within the channel. We constructed two new peptides: one with a Cys residue at the start of the sequence (Ac-**C**LPHPLQRL-amide, called C-1) and one following the 8-residue inhibitor (Ac-LPHPLQRL**C**-amide, called C9). Our models suggest that Glu^{174} is close to Leu^{211} (Fig. 6*B*), which corresponds to the first residue within P8. Hence, we predict that E174C is better situated to cross-link to C-1, which has the Cys adjacent to the first residue in P8, rather than C9, which has the Cys at the opposite end of the peptide. We individually mutated Glu^{173} and Glu^{174} to Cys and treated oocytes expressing these mutants with MTS-4-MTS in the presence of amiloride. After washing away free MTS-4-MTS, C-1 or C9 peptides were added and then washed out to assess the reversibility of peptide inhibition (Fig. 6, *D* and *E*). We observed that a significant component of channel activity remained inhibited in MTS-4-MTS-treated oocytes expressing E174C following a brief exposure and washout of the C-1 peptide as predicted by our model. In contrast, we observed nearly complete reversibility of E174C channel activity following washout of the C9 peptide. A lack of complete reversibility following washout of the C9 peptide may reflect a modest time-dependent decrease in channel activity that we frequently observe. We also observed nearly complete reversibility of E173C channel activity following washout of the C-1 or C9 peptides.

Therefore, these data are consistent with selective cross-linking of E174C to a Cys residue preceding P8 (*i.e.* C-1), confirming our model-based prediction and the results of the Trp scan. Taken together, these results illustrate that our models have gross overall features that are most likely correct.

FIGURE 4. **Building models of α ENaC from the resolved ASIC1 structure and P8 inhibition data.** *A*, initial model alignments between α ENaC and ASIC1 for the finger domain. Observed secondary structure for ASIC1 and predicted secondary structure for α ENaC are shown. *Blue* and *red* indicate β-strands and α-helices, respectively, with strong consensus. *Turquoise* and *pink* indicate β-strands and α-helices, respectively, with weak consensus. The four different finger domain alignments used to generate initial models are highlighted in *green*. Identities (*dark gray background*, *white type*), strong similarity (*light gray background*, *boldface type*), and weak similarity (*light gray background*) are indicated. *B*, histogram of scores for models built from each selected initial model. Z-scores were calculated and summed for the MODELLER score, 211–218 solvent accessibility, and ability to satisfy our distance constraints for each model. Lower values are better. The initial model used and median scores are indicated in each *panel*. *C*, clustering diagram of 20,000 models generated from selected initial models. The area of each node is proportional to the size the cluster it represents. Node *colors* indicate the initial model used for all the models of that cluster. Internode distances reflect r.m.s. deviation between cluster centroids. The clustering diagram was made using Cytoscape (34) using a force-directed layout weighted by intercluster centroid r.m.s. deviation.

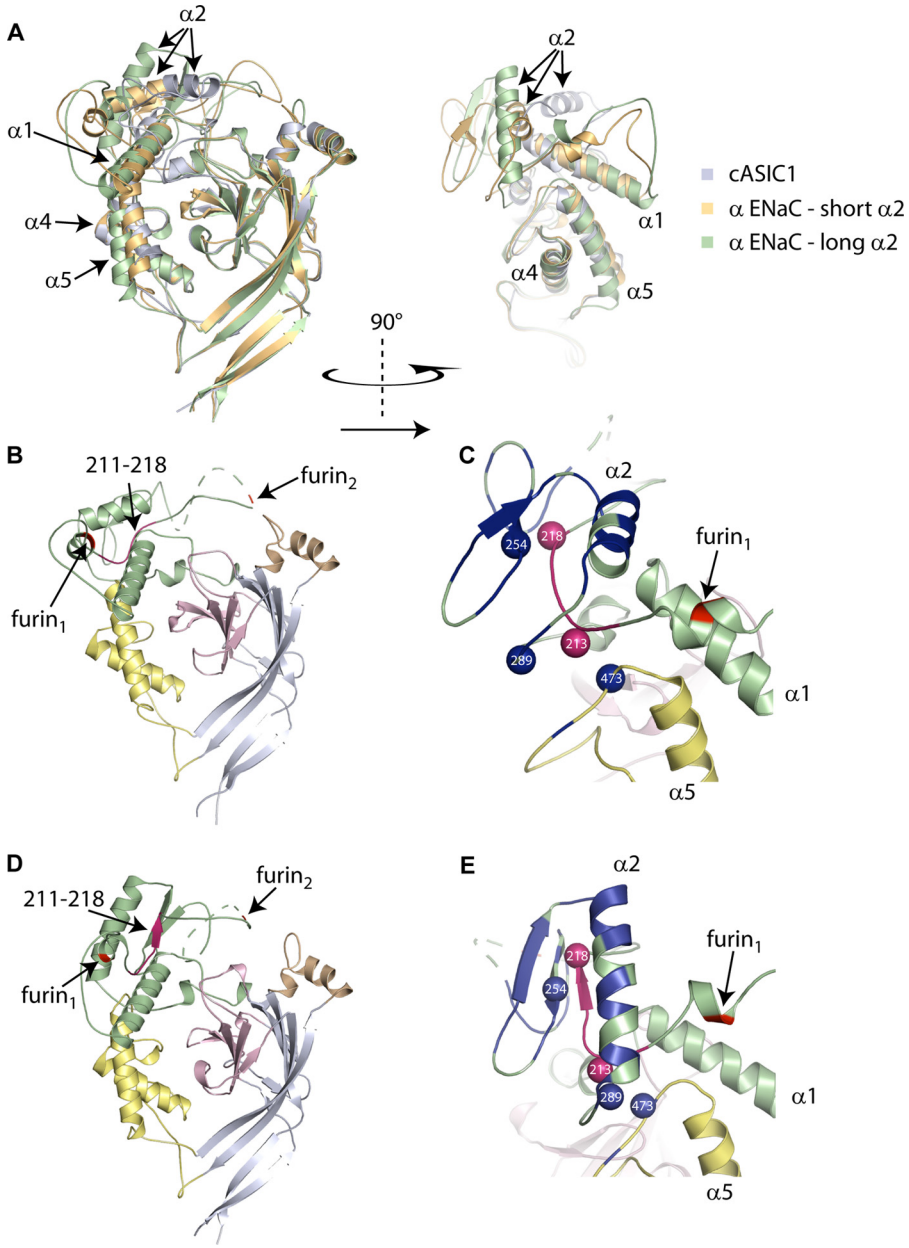

FIGURE 5. **α ENaC models.** α ENaC models with either a short α2 (*B* and *C*) or a long α2 (*D* and *E*) are presented individually or superimposed with ASIC1 (*A*). *B–E*, highlighted are the 211–218 tract, corresponding to P8 (*pink*), furin cleavage sites (*red*), and predicted disordered tract (*dashed line*). The second furin cleavage site is not visible in *C* and *E*. *C* and *E*, residues that affected P8 inhibition (*blue*) were found in or just after α2, in the loop that precedes α2, and at the top of the thumb. The three identified pairwise interactions between P8 (*red spheres*) and α ENaC (*blue spheres*) are indicated within the uncleaved structures. These models feature a small anti-parallel β-sheet in the finger domain (which includes residue 254) with which the 211–218 tract may interact.

Normal Mode Analysis of the α ENaC Model—To further investigate the consequence of P8 binding in our model, we performed normal mode analysis on the long α2 model using the ANM (Anisotropic Network Model) Web server (35). Normal mode analysis is a computational framework that determines the equilibrium movements (or vibrations) of proteins around a starting minimized conformation (*e.g.* a closed state) on the long time scale and is inherently compatible with the low resolution nature of our models. Normal mode analysis has been extensively applied to the study of membrane proteins (see Ref. 47 for a comprehensive list of studies), but to date, the majority of studies have ignored the effect of the membrane. Given the limitations of the ANM Web server, we also ignored the influence of the membrane. It is generally thought that the slowest modes, which we analyze here, are qualitatively insensitive to such perturbations (47). Before carrying out the calculations, we used MODELLER to create a trimer of α subunits and add the transmembrane helices using ASIC1 (23) as a template. We also removed the predicted disordered loop in the finger (residues 230–244) and the 26-residue inhibitory tract. To determine the influence of P8, we added the corresponding residues back to a separate model. Therefore, one model lacks P8, and the other has P8 placed according to our model.

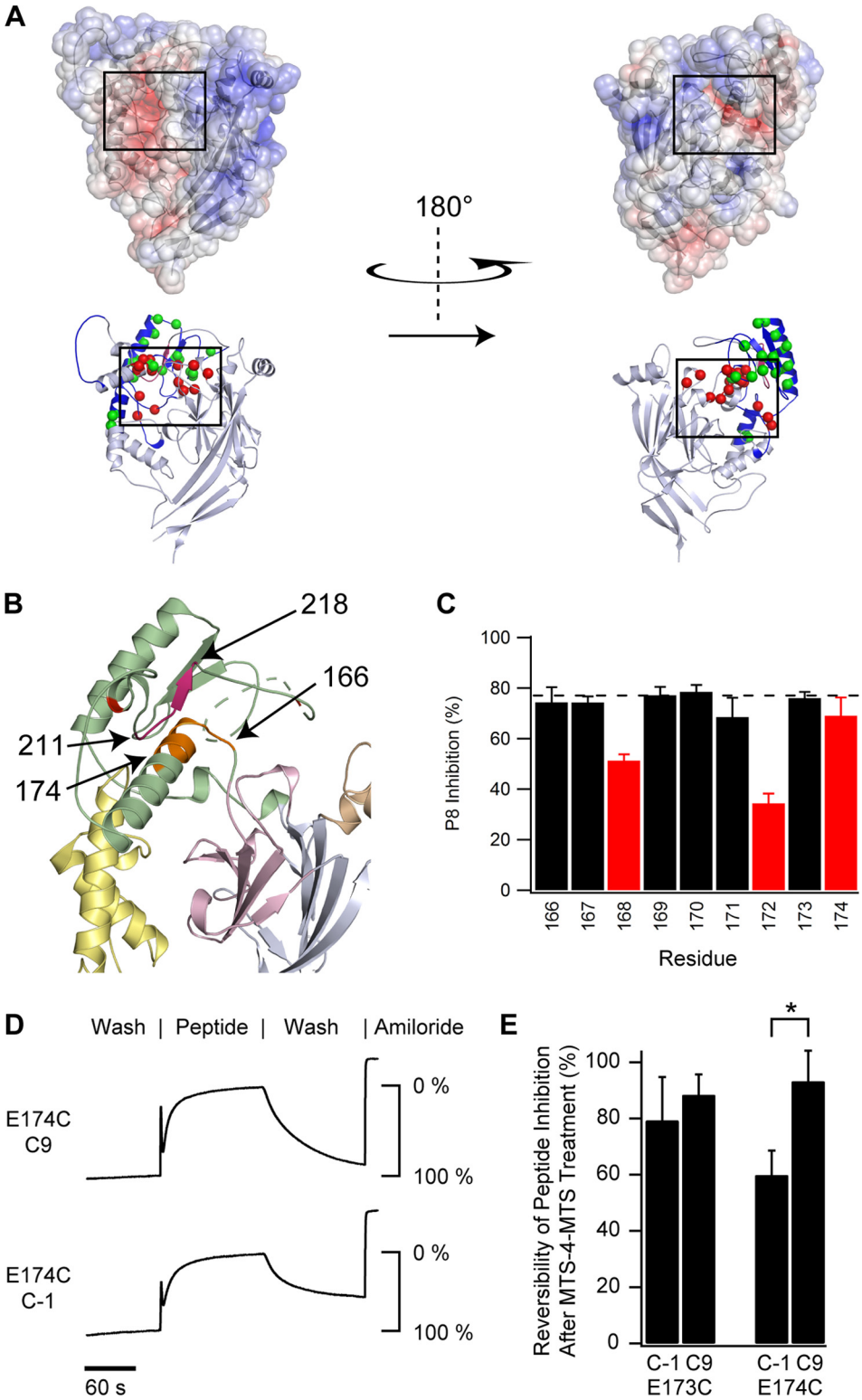

FIGURE 6. **Predictions based on the α ENaC models.** *A*, solvent-accessible surface of long α2 model with relatively basic (*blue*) and acidic (*red*) surfaces highlighted. The acidic region at the finger/thumb/β-ball junction is *boxed*, with acidic residues in the region highlighted in the schematic (*red spheres*). All sites that were mutated are indicated (*blue ribbon*). Sites where mutations altered Na^+ self-inhibition (22), as determined by analysis of variance with a Newman-Keuls *post hoc* test, are highlighted (*green spheres*). *B*, the best scoring α ENaC models consistently placed P8-corresponding residues 211–218 (*pink*) in close proximity to residues 166–174 (*orange*). *C*, residues 166–174 were individually mutated to Trp and assayed for effects on P8 inhibition. Data were included with all other Trp mutants in non-linear mixed model analysis to determine *p* values *versus* wild-type ENaC (22). Values are mean ± S.D. (*error bars*), and *red bars* indicate $p < 0.0001$ *versus* wild-type ENaC. *D* and *E*, reversibility of peptide inhibition following treatment with MTS-4-MTS. αE173C and αE174C were expressed with wild type β and γ ENaC subunits in *X. laevis* oocytes. ENaC currents were measured by two-electrode voltage clamp at −60 mV. Oocytes were treated with 10 μM MTS-4-MTS for 2 min in the presence of 20 μM amiloride, after which oocytes were washed and treated as shown in the representative recordings in *D*. The reversibility of peptide inhibition was determined by comparing the current at the end of peptide washout to the currents both prior to and after peptide addition (*i.e.* reversibility of the peptide-inhibitable component of the whole cell Na^+ current). *E*, the mean ± S.D. of 6 experiments per condition are shown. *, $p < 0.01$ by Student's *t* test.

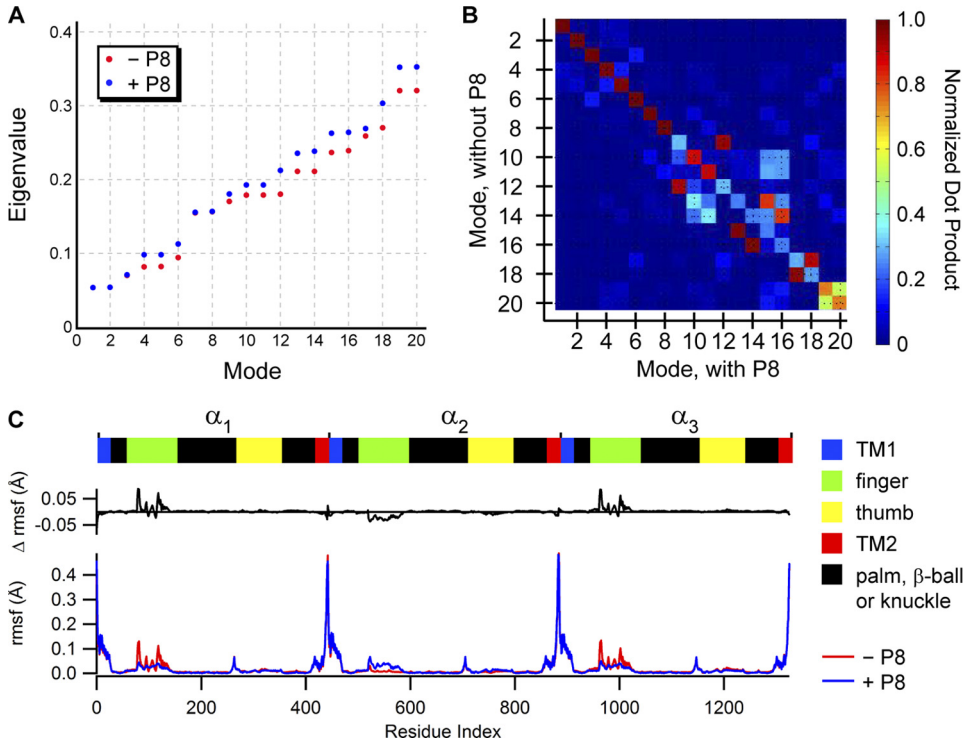

FIGURE 7. **Normal mode analysis of a trimer of ENaC α subunits with a long α2, including transmembrane (*TM*) helices, with and without P8.** *A*, eigenvalues of the first 20 modes in the presence or absence of P8 were computed as discussed under "Experimental Procedures" using the default cut-off distance of 15 Å and a spring constant of 1 kcal/mol/Å^2. *B*, normalized dot product of first 20 modes. *C*, the root mean square fluctuation (*rmsf*) of mode 9 with P8 (*blue*) and mode 12 without P8 (*red*) and their difference (Δ*rmsf*) are shown. Each subunit and the domains within each subunit are indicated. Amplitudes were generated assuming the molecule was at room temperature.

We then compared the lowest 20 modes, which correspond to the largest motions and the slowest time scales, with and without P8 to identify changes brought about by the peptide (Fig. 7, *A* and *B*). Within the normal mode framework, one can determine the similarity between modes by calculating to what degree the deformations described by those modes are co-linear. We therefore took the absolute value of the scalar product of the *i*th eigenvector from the structure with P8, v_i, with the *j*th eigenvector from the structure lacking P8, w_j. Eigenvectors obtained from the structure with P8 are longer than those without P8 due to the presence of additional atoms. To carry out the dot products, we removed the elements corresponding to the P8 atoms from the longer eigenvectors, normalized all of the eigenvectors from both structures, and then calculated the dot products of all eigenvectors containing P8 with all eigenvectors lacking P8 to construct the matrix in Fig. 7*B*. If the two eigenvectors are co-linear, the absolute value of the scalar product is 1 (0 if they are orthogonal). Because the eigenvectors span spaces of different dimension, this method does not strictly inform us about the true overlap between modes. However, this procedure unambiguously informs us as to which modes to investigate further.

For the majority of modes, the presence of P8 made little difference, with the first three modes nearly identical to that found for ASIC1 (48). 18 of these modes were nearly identical with and without the peptide. However, the eigenvalue orders of four modes were switched in the presence of the peptide. For all but modes 9 and 12, these switches involve small changes in the eigenvalue of degenerate modes. Additionally,

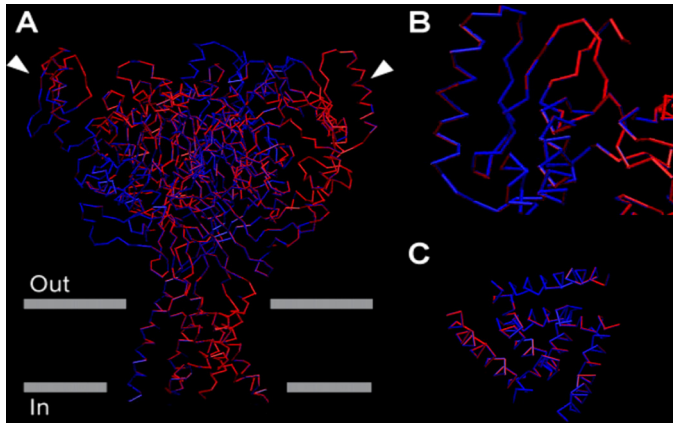

FIGURE 8. **Superposition of normal mode 9 with P8 (*blue*) and mode 12 without P8 (*red*).** Shown is a still view from supplemental Movie S1. The atomic coordinates of each model were displaced in small increments according to their respective eigenvector generated from the ANM server. We carried out the displacements at room temperature, which set the amplitude of each mode. However, we scaled the displacements by a multiplicative factor of 7 in order to visualize the motions in each movie. *A*, a profile view of the channel with the transmembrane domain at the bottom. The *arrows* indicate the finger domains where the largest difference in motion occurs. The *bars* indicate the approximate position of the membrane. *B*, *zoomed-in view* of the finger domain. *C*, a view of the channel from the cytoplasm along the channel's long axis with the extracellular domain removed.

there is a moderate mixing of modes 19 and 20. We visualized all of these modes, and we only found compelling differences when comparing mode 9 with the inhibitory peptide and mode 12 without the peptide. The frequency of both modes is identical, but the finger domain near the P8 binding site un-

dergoes much larger motions in the absence of P8 (Figs. 7*C* and 8 and supplemental Movie S1). Additionally, the motion in the transmembrane domain is identical for both modes and undergoes a twisting motion about the long axis of the molecule that may lead to channel opening, resembling mode 3 for both our model and ASIC1 (48). This result suggests that peptide binding damps out fluctuations at the finger-thumb interface that are coupled with potential conformational changes in the transmembrane region.

DISCUSSION

The gating of members of the ENaC/degenerin family of ion channels is influenced by extracellular cues. The resolved ASIC1 structure revealed an intricate organization of the extracellular domains of these channels and highlighted the importance of the connection between the finger and thumb domains, where it was suggested that proton binding drives channel opening by enhancing the relative movements of these domains (1). The regulatory control of ENaC gating involves a number of extracellular factors, including Na^+ (7), H^+ (49), Cl^- (50), the proteolytic release of inhibitory tracts from the α and γ subunits (9, 11), and shear stress (51). To date, very little is known about how these external factors gate these channels or what motions give rise to channel opening or closing. Given the roles of a variety of external factors in modulating the gating of members of the ENaC/degenerin family, it is not surprising that parts of the gating machinery are conserved, whereas others appear to have evolved to respond to a diverse set of cues. Specifically, the highly variable finger domain, the bulk of which is attached to the rest of the molecule at two nearby points in ASIC1 (see Fig. 1), is poised to be a modular domain that helps provide functional differentiation for ENaC/degenerin family members. For ASIC1, finger residues are probably involved in sensing protons (1). For ENaC, we showed that the finger is crucial to channel regulation by proteases and observed that mutations in the finger have large effects on Na^+ self-inhibition (6, 22, 52). This underlines the importance of the finger domain to understanding the diversity of functions in the ENaC/degenerin family.

The models of α ENaC presented here rationalize a large set of data for P8 inhibition while still retaining a strong structural identity with ASIC1. Based on our model, P8 produces its inhibitory effect by occupying a binding site largely defined within the finger but also at the thumb-finger interface. Normal mode analysis of our model suggests that P8 reduces motions in the finger domain that are coupled with motions in the pore that may be associated with channel gating. These findings suggest a mechanism for P8 inhibition of ENaC and, by extension, for channel activation by furin excision of the α subunit inhibitory tract.

With regard to the inhibition of channel gating by external Na^+ (*i.e.* Na^+ self-inhibition), inspection of a surface charge map of α ENaC revealed a striking acidic region at the junction of the finger, thumb, and β-ball domains (Fig. 6*A*), analogous to ASIC1 (1). Since differences in the finger domains of ENaC/degenerin family members may account for much of their functional differentiation, we speculate that residues in this acidic region are involved in Na^+-self-inhibition. Consistent with this hypothesis, mutations that affected Na^+ self-inhibition (*green* in Fig. 6*A*) are in close proximity to the acidic residues in this region (*red* in Fig. 6*A*).

To create models of α ENaC, we used ASIC1 as a template for comparative modeling and used P8 binding data to derive structural information about the most divergent aspect of their structures. An important feature with regard to our present models is that residues in the late finger and the top of the thumb contact the inhibitory tract. This feature is present in nearly all of our constructed models, and it is derived from data that are internally consistent with double mutant cycle experiments (22) and the tethered peptide-dislodging assay (Fig. 2). Nonetheless, there are limitations of comparative modeling (31). We used C_α-C_α distance restraints to complement homology-based restraints. Although we restrained 36% of unaligned finger residues, the restrained residues fell within two tracts: 211–218 and 70% of residues in 239–289. The high density of restraints supports higher confidence in the parts of the model containing the latter half of the finger (α2 and the two preceding β-strands) and particularly in the placement of part of the 211–218 tract at the thumb-finger interface because C_α-C_α restraints there complement homology-based restraints in the thumb. The lack of restraints for the loop connecting α1 to 211–218 and the 20-residue loop after 218 (containing the predicted disordered region) suggest low confidence in their presented structures. Although we were unable to constrain the solvent accessibility of residues, such as those corresponding to P8, the furin cleavage sites, or *N*-glycosylation sites during model building, these residues are solvent-accessible in our models. Due to the lack of a suitable template for most of the finger domain, we observed an initial model bias in the gross arrangement of finger domain helices when generating models. We attempted to minimize this bias by using 12 different initial models and increasing the initial model randomization parameter in MODELLER from the default value of 4 Å to 20 Å. In the absence of a resolved crystallographic structure of ENaC, we expect that future experiments will allow us to derive additional distance constraints that give us more confidence in our selected structural ENaC models.

Jasti *et al.* (1) have proposed that relative movements between the thumb and finger domains translate binding events in the finger and thumb domains to gating motions in the pores of these channels. Although mutations in the finger and/or thumb domains have been shown to affect the gating behavior of ASICs in response to external acidification (1) as well as the gating behavior of ENaCs in response to external Na^+ and Cl^- (5, 50), there is no direct evidence supporting the hypothesis that relative movements of the thumb and finger domains modulate channel gating in response to external cues. Our findings regarding the P8 binding site support this hypothesis and suggest that non-cleaved channels are stabilized in a closed state in the presence of external Na^+ (12) by interactions between the α subunit inhibitory tract and specific finger and thumb domain residues that restrict the relative mobility of these domains. Furin processing of the α sub-

unit releases the inhibitory tract and allows for larger motions of the thumb and finger domains, translating into changes in channel gating.

Acknowledgments—We thank Christos Argyropoulos for performing non-linear mixed regression model analysis of our data and Andrew P. VanDemark and Ivet Bahar for helpful discussions.

REFERENCES

1. Jasti, J., Furukawa, H., Gonzales, E. B., and Gouaux, E. (2007) *Nature* **449,** 316–323
2. Staruschenko, A., Adams, E., Booth, R. E., and Stockand, J. D. (2005) *Biophys. J.* **88,** 3966–3975
3. Canessa, C. M., Schild, L., Buell, G., Thorens, B., Gautschi, I., Horisberger, J. D., and Rossier, B. C. (1994) *Nature* **367,** 463–467
4. Sheng, S., Johnson, J. P., and Kleyman, T. R. (2008) in *The Kidney: Physiology and Pathophysiology* (Alpern, R. J., and Hebert, S. C., eds) pp. 743–768, 4th Ed., Elsevier Publishing, Philadelphia, PA
5. Maarouf, A. B., Sheng, N., Chen, J., Winarski, K. L., Okumura, S., Carattino, M. D., Boyd, C. R., Kleyman, T. R., and Sheng, S. (2009) *J. Biol. Chem.* **284,** 7756–7765
6. Sheng, S., Bruns, J. B., and Kleyman, T. R. (2004) *J. Biol. Chem.* **279,** 9743–9749
7. Fuchs, W., Larsen, E. H., and Lindemann, B. (1977) *J. Physiol.* **267,** 137–166
8. Kleyman, T. R., Carattino, M. D., and Hughey, R. P. (2009) *J. Biol. Chem.* **284,** 20447–20451
9. Carattino, M. D., Sheng, S., Bruns, J. B., Pilewski, J. M., Hughey, R. P., and Kleyman, T. R. (2006) *J. Biol. Chem.* **281,** 18901–18907
10. Hughey, R. P., Bruns, J. B., Kinlough, C. L., Harkleroad, K. L., Tong, Q., Carattino, M. D., Johnson, J. P., Stockand, J. D., and Kleyman, T. R. (2004) *J. Biol. Chem.* **279,** 18111–18114
11. Bruns, J. B., Carattino, M. D., Sheng, S., Maarouf, A. B., Weisz, O. A., Pilewski, J. M., Hughey, R. P., and Kleyman, T. R. (2007) *J. Biol. Chem.* **282,** 6153–6160
12. Sheng, S., Carattino, M. D., Bruns, J. B., Hughey, R. P., and Kleyman, T. R. (2006) *Am. J. Physiol. Renal Physiol.* **290,** F1488–F1496
13. Carattino, M. D., Passero, C. J., Steren, C. A., Maarouf, A. B., Pilewski, J. M., Myerburg, M. M., Hughey, R. P., and Kleyman, T. R. (2008) *Am. J. Physiol. Renal Physiol.* **294,** F47–F52
14. Passero, C. J., Carattino, M. D., Kashlan, O. B., Myerburg, M. M., Hughey, R. P., and Kleyman, T. R. (2010) *Am. J. Physiol. Renal Physiol.* **299,** F854–F861
15. Passero, C. J., Mueller, G. M., Rondon-Berrios, H., Tofovic, S. P., Hughey, R. P., and Kleyman, T. R. (2008) *J. Biol. Chem.* **283,** 36586–36591
16. Adebamiro, A., Cheng, Y., Rao, U. S., Danahay, H., and Bridges, R. J. (2007) *J. Gen. Physiol.* **130,** 611–629
17. Myerburg, M. M., McKenna, E. E., Luke, C. J., Frizzell, R. A., Kleyman, T. R., and Pilewski, J. M. (2008) *Am. J. Physiol. Lung Cell. Mol. Physiol.* **294,** L932–L941
18. Myerburg, M. M., Butterworth, M. B., McKenna, E. E., Peters, K. W., Frizzell, R. A., Kleyman, T. R., and Pilewski, J. M. (2006) *J. Biol. Chem.* **281,** 27942–27949
19. Mall, M., Grubb, B. R., Harkema, J. R., O'Neal, W. K., and Boucher, R. C. (2004) *Nat. Med.* **10,** 487–493
20. Passero, C. J., Hughey, R. P., and Kleyman, T. R. (2010) *Curr. Opin. Nephrol Hypertens.* **19,** 13–19
21. Kastner, C., Pohl, M., Sendeski, M., Stange, G., Wagner, C. A., Jensen, B., Patzak, A., Bachmann, S., and Theilig, F. (2009) *Am. J. Physiol. Renal Physiol.* **296,** F902–F911
22. Kashlan, O. B., Boyd, C. R., Argyropoulos, C., Okumura, S., Hughey, R. P., Grabe, M., and Kleyman, T. R. (2010) *J. Biol. Chem.* **285,** 35216–35223
23. Gonzales, E. B., Kawate, T., and Gouaux, E. (2009) *Nature* **460,** 599–604
24. Kellenberger, S., and Schild, L. (2002) *Physiol. Rev.* **82,** 735–767
25. Larkin, M. A., Blackshields, G., Brown, N. P., Chenna, R., McGettigan, P. A., McWilliam, H., Valentin, F., Wallace, I. M., Wilm, A., Lopez, R., Thompson, J. D., Gibson, T. J., and Higgins, D. G. (2007) *Bioinformatics* **23,** 2947–2948
26. Ouali, M., and King, R. D. (2000) *Protein Sci.* **9,** 1162–1176
27. Baldi, P., Brunak, S., Frasconi, P., Soda, G., and Pollastri, G. (1999) *Bioinformatics* **15,** 937–946
28. Jones, D. T. (1999) *J. Mol. Biol.* **292,** 195–202
29. Rost, B., Yachdav, G., and Liu, J. (2004) *Nucleic Acids Res.* **32,** W321–326
30. Cole, C., Barber, J. D., and Barton, G. J. (2008) *Nucleic Acids Res.* **36,** W197–201
31. Eswar, N., Webb, B., Marti-Renom, M. A., Madhusudhan, M. S., Eramian, D., Shen, M. Y., Pieper, U., and Sali, A. (2006) *Curr. Protoc. Bioinformatics*, Chapter 5, Unit 5.6
32. Guex, N., and Peitsch, M. C. (1997) *Electrophoresis* **18,** 2714–2723
33. Feig, M., Karanicolas, J., and Brooks, C. L., 3rd (2004) *J. Mol. Graph. Model.* **22,** 377–395
34. Shannon, P., Markiel, A., Ozier, O., Baliga, N. S., Wang, J. T., Ramage, D., Amin, N., Schwikowski, B., and Ideker, T. (2003) *Genome Res.* **13,** 2498–2504
35. Eyal, E., Yang, L. W., and Bahar, I. (2006) *Bioinformatics* **22,** 2619–2627
36. Atilgan, A. R., Durell, S. R., Jernigan, R. L., Demirel, M. C., Keskin, O., and Bahar, I. (2001) *Biophys J.* **80,** 505–515
37. Baker, D., and Sali, A. (2001) *Science* **294,** 93–96
38. Bianchi, L., and Driscoll, M. (2002) *Neuron* **34,** 337–340
39. Abramson, J., and Wright, E. M. (2009) *Curr. Opin Struct. Biol.* **19,** 425–432
40. Sheng, S., Maarouf, A. B., Bruns, J. B., Hughey, R. P., and Kleyman, T. R. (2007) *J. Biol. Chem.* **282,** 20180–20190
41. Chothia, C., and Lesk, A. M. (1986) *EMBO J.* **5,** 823–826
42. Stockand, J. D., Staruschenko, A., Pochynyuk, O., Booth, R. E., and Silverthorn, D. U. (2008) *IUBMB Life* **60,** 620–628
43. Reddy, B. V., and Kaznessis, Y. N. (2007) *J. Biosci.* **32,** 929–936
44. Ward, J. J., Sodhi, J. S., McGuffin, L. J., Buxton, B. F., and Jones, D. T. (2004) *J. Mol. Biol.* **337,** 635–645
45. Sippl, M. J. (1993) *Proteins* **17,** 355–362
46. Wiederstein, M., and Sippl, M. J. (2007) *Nucleic Acids Res.* **35,** W407–W410
47. Bahar, I. (2010) *J. Gen. Physiol.* **135,** 563–573
48. Yang, H., Yu, Y., Li, W. G., Yu, F., Cao, H., Xu, T. L., and Jiang, H. (2009) *PLoS Biol.* **7,** e1000151
49. Collier, D. M., and Snyder, P. M. (2009) *J. Biol. Chem.* **284,** 792–798
50. Collier, D. M., and Snyder, P. M. (2009) *J. Biol. Chem.* **284,** 29320–29325
51. Carattino, M. D., Sheng, S., and Kleyman, T. R. (2004) *J. Biol. Chem.* **279,** 4120–4126
52. Winarski, K. L., Sheng, N., Chen, J., Kleyman, T. R., and Sheng, S. (2010) *J. Biol. Chem.* **285,** 26088–26096